A FINITE ELEMENT APPROXIMATION OF STEADY FLOW THROUGH A ROTATING NON-ALIGNED STRAIGHT TUBE

W. P. NORONHA* AND J. BERMAN†

Department of Chemical Engineering, University of Kentucky, Lexington, Kentucky 40506–0046. U.S.A.

SUMMARY

A finite element solution is developed for a penalty function formulation of the equations which govern the steady motion of a Newtonian fluid through a pipe that rotates about an axis not parallel to its own. The motion in this system is driven by the Coriolis acceleration, which has components in the axial direction as well as in the transverse plane of the pipe. The relative magnitudes of these components significantly affect the qualitative and quantitative nature of the primary and secondary flow field. The present results compare favourably with those of previously reported experimental and theoretical studies over a wide range of flow regimes.

KEY WORDS   Coriolis   Rotating Tube   Finite Element   Fluid Mechanics

INTRODUCTION

Low Reynolds number tubular heat and mass exchange devices are of great importance to the automobile, aerospace, chemical process and medical device industries. One method of enhancing the transport efficiency of such devices is via the superposition of laminar secondary circulations upon the primary velocity distribution. The resulting transverse velocity components lead to fluid mixing and hence augmented transport within the tubular lumen. As an example, the often studied problem of transport in helically coiled tubes uses centrifugal accelerations to achieve increased rates of heat and mass transfer. Alternative methods of promoting viscous cross-sectional fluid mixing include the use of flow obstructions such as baffles and screens, oscillating systems[1] and rotating devices.[2,3]

In many applications, however, design limitations preclude the use of these established transport enhancement techniques. For example, a clinically practical extracorporeal tubular blood oxygenator might require several thousand tubes in parallel. Thus, an oxygenator consisting of coiled tubes would be of limited utility, owing to its low packing density and correspondingly high priming volume. Recently, Berman and Mockros[4-6] have proposed the use of rotating non-aligned straight tubes as a method of improving mass transfer in low Reynolds number tubular devices. This new technique consists of a straight tube that rotates about an axis not parallel to its own. Secondary motions appear in the cross-section of the tube as a result of the Coriolis acceleration which arises with rotation. These secondary motions are qualitatively similar to those that appear

---

*Present address: Department of Engineering Science & Applied Mechanics, University of Tennessee, TN, U.S.A.
†Author to whom correspondence should be addressed.

in helically coiled tubes as a result of the centrifugal acceleration and identical to those which develop in a straight tube rotating about an axis perpendicular to its own.

Berman and Mockros[6] have demonstrated, both theoretically and experimentally, that a very small non-alignment of the tube (with respect to the axis of rotation), in the presence of sufficiently rapid angular motion, can lead to significant mass transfer enhancement relative to a stationary straight tube. This result suggests that exchange units incorporating this technique can be fabricated by slightly twisting a bank of parallel straight tubes, constrained between two common headers, and rotating the bank about its original longitudinal axis. With appropriate angular velocities such devices can exhibit the transport advantages of coiled tubes coupled with the design advantages of straight tube units.

A theoretical description of heat or mass transfer into fluids flowing steadily through a rotating non-aligned straight tube requires an accurate solution of the governing Navier–Stokes equation. The literature contains approximations to this solution that are valid for either small or large Coriolis disturbances. Berman and Mockros[5] have developed a third-order regular perturbation approximation of the primary and secondary flow fields, in a rotating non-aligned straight tube, which is valid only for sufficiently small Coriolis accelerations. Their analysis is an extension of Barua's[7] study of flow through a straight pipe that rotates about an axis perpendicular to its own. Benton[8] used similar techniques to characterize the motion of a fluid flowing through a straight pipe subject to the weak Coriolis effects of the earth's rotation. The primary result of these studies has been to demonstrate that the flow fields which arise when a straight pipe is 'slowly' rotated about an axis that is not parallel to its own are very similar to those that occur in low Dean number flow through coiled tubes of negligible coil ratio. Thus, flow in the transverse plane of the tube consists of a weak double-vortex secondary flow which, under appropriate conditions, can significantly distort the axial velocity distribution.

In the limit of small Coriolis accelerations the primary and secondary velocity distributions depend on the values of two fluid mechanical parameters. The first of these parameters, N_A^2, represents the square of the ratio of Coriolis to viscous forces and is analogous to the coil ratio in the coiled tube problem. This parameter is defined as

$$N_A^2 = \left[\frac{4\Omega a^2 \sin \alpha}{v} \right]^2, \tag{1}$$

in which a is the radius of the tube, Ω is its angular velocity, v is the kinematic viscosity of the flowing fluid and α is the angle of non-alignment of the tube (defined in Figure 1). The second parameter, ReN_A, is the product of the square root of the first parameter and the axial Reynolds number:

$$Re = \frac{2a\bar{W}}{v}, \tag{2}$$

in which $\bar{W}$ is the average axial velocity in the cross-section of the tube. This parameter is similar to the Dean number. Berman and Mockros[5] estimate that their solution is valid for $N_A \lesssim 40$ and $ReN_A \lesssim 780$. (Note that Berman and Mockros[5] used a slightly different scaling factor in their solution. Instead of N_A they used N_α in which $N_A = 192N_\alpha$.)

Mori and Nakayama[9] used a boundary layer analysis to study momentum and heat transfer in rotating straight pipes for $Re/N_A \gg 1$ and $ReN_A \gg 1$. Their approximate theoretical results, however, fail to accurately predict experimental head loss measurements. Ito and Nanbu[10] developed an alternative solution to the same problem. Their theoretical results are in good qualitative agreement with their friction drop measurements for $Re/N_A > 2$. Mansour[11] used a computer to extend the series solution for a slowly rotating pipe in terms of a single similarity

parameter of the form ReN_A. This solution was said to be valid for all values of ReN_A in the limit $N_A \rightarrow 0$. Furthermore, the friction ratio in a slowly rotating pipe was found to grow asymptotically as the 1/8 power of ReN_A and not as the 1/4 power, as was reported by Ito and Nanbu.[10] Mansour[11] suggests that one explanation for this discrepancy may be due to a bifurcation of the solution at large values of ReN_A.

Benton and Boyer[12] investigated flow in a rotating pipe of arbitrary cross-section in the limit of rapid rotation, $N_A \gg 1$, and small axial velocities, $Re/N_A \ll 1$. Their results indicate that the flow consists of a viscous boundary layer surrounding an inviscid core. They concluded that the flow in the interior of the pipe is geostrophic and that inertial effects may be neglected everywhere. Ito and Nanbu[10] studied the same problem for a circular geometry, and they present results that are in good agreement with those of Benton and Boyer.[12]

Several investigators have employed numerical methods to solve this problem in flow regimes not accessible to analytical techniques. Duck[13] developed a numerical solution, using a Fourier decomposition, for flow through a rotating straight pipe of circular cross-section. These results, however, are valid only for a small range of the governing parameters. Speziale[14] used finite difference techniques to study flow through rotating ducts of rectangular cross-section for moderate to relatively rapid rotation rates. He demonstrated that, as the rotation rate is increased, for a duct with an aspect ratio of two the secondary flow splits from a symmetric system of two counter-rotating vortices into an asymmetric system of four counter-rotating vortices. As N_A is further increased, the secondary flow restabilizes to a distorted vortex pair and the axial distribution assumes a Taylor–Proudman configuration. Recently, Kheshgi and Scriven[15] have solved the same problem, for a square duct, using the penalty/Galerkin/finite element method. Their results show that the two-vortex solution bifurcates into a four-vortex solution as Re/N_A is increased for fixed values of $N_A \gg 1$. These two additional vortices, however, appear on the opposite side of the channel from where Speziale[14] predicts that they should arise.

All of these previously reported analytical studies are valid only for flow regimes that are driven either by very small or very large Coriolis accelerations. The non-linearity of the governing system of coupled partial differential equations precludes the use of analytical techniques to describe the fluid motion in intermediate flow regimes. Solutions in these regimes are best approximated using numerical techniques. The present work is a finite element analysis of the steady, laminar, fully developed flow of an incompressible Newtonian fluid through a rotating non-aligned straight tube of circular cross-section. To our knowledge this is the first study to use finite element techniques to solve this problem. Since this study was completed, a parallel effort by Kheshgi and Scriven[15] has appeared. Kheshgi and Scriven treated the case of a tube of square cross-section. The results of this analysis compare favourably with the perturbation solution of Berman and Mockros[5] in the limit of mild Coriolis disturbances as well as the experimental friction drop measurements of Ito and Nanbu[10] for large Coriolis effects.

GOVERNING EQUATIONS

In the current study a Cartesian reference system has been employed. Mapping a curved domain in a rectangular system presents little difficulty since the finite element technique enables the use of curved elements. The non-inertial co-ordinate system is defined in Figure 1. A Newtonian fluid flows steadily through a straight pipe of radius a, that rotates at a constant angular velocity Ω about an axis orientated at a non-zero angle, α, relative to the centreline of the pipe. In the limiting case of $\alpha = 0°$ the pipe rotates about an axis parallel to its own, whereas rotation about a perpendicular axis is characterized by a non-alignment angle of 90°. In general, the tube may be displaced a constant distance, R, from the axis of rotation. The dimensionless equations that
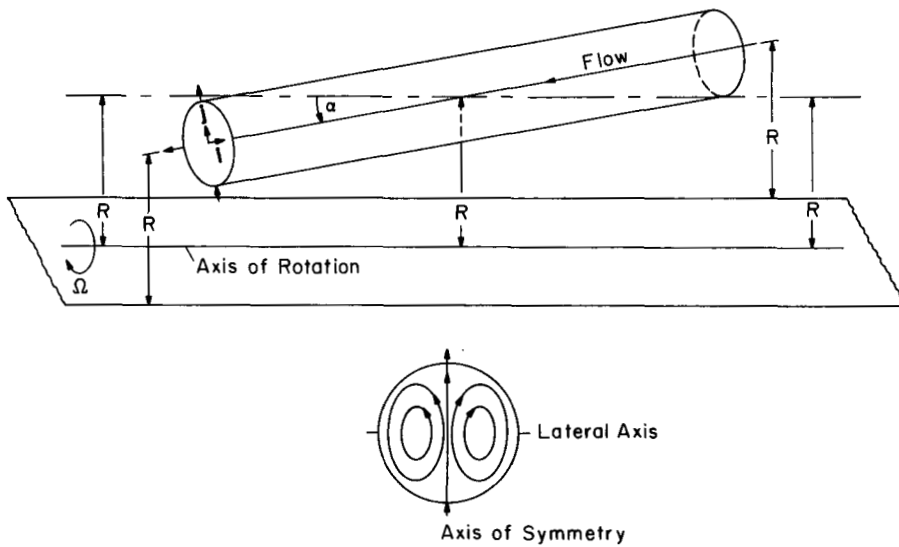
Figure 1. The rotating non-aligned straight tube geometry

govern the steady motion of a fluid through this system are those which ensure conservation of mass and momentum:

$$\frac{\partial u}{\partial x} + \frac{\partial v}{\partial y} = 0, \tag{3}$$

$$u\frac{\partial u}{\partial x} + v\frac{\partial u}{\partial y} = \frac{\partial^2 u}{\partial x^2} + \frac{\partial^2 u}{\partial y^2} - \frac{\partial P}{\partial x}, \tag{4}$$

$$u\frac{\partial v}{\partial x} + v\frac{\partial v}{\partial y} - \frac{N_A}{2}w = \frac{\partial^2 v}{\partial x^2} + \frac{\partial^2 v}{\partial y^2} - \frac{\partial P}{\partial y} \tag{5}$$

and

$$u\frac{\partial w}{\partial x} + v\frac{\partial w}{\partial y} + \frac{N_A}{2}v = \frac{\partial^2 w}{\partial x^2} + \frac{\partial^2 w}{\partial y^2} + 4G, \tag{6}$$

in which P is a modified pressure and u, v and w are x, y and z components of velocity, respectively. These variables are non-dimensionalized as follows (an asterisk denotes a dimensional variable):

$$(u, v, w) = (u^*, v^*, w^*)a/v, \tag{7}$$

$$(x, y) = (x^*, y^*)/a, \tag{8}$$

and

$$G = -\frac{\partial P^*}{\partial Z^*}\frac{a^3}{4\rho v^2}. \tag{9}$$

Thus, the steady laminar motion of a fluid through a rotating non-aligned straight tube is characterized by two dimensionless fluid mechanical parameters. The first of these parameters, N_A, serves as an angular Reynolds number, whereas the second parameter, G, represents the pressure drop across the system.

In the limiting case of flow through a straight pipe rotating about an axis that is parallel to its own (i.e. for $\alpha = 0°$) the Coriolis acceleration and hence the secondary motion vanishes. Thus, in this limit, the axial velocity profile is a paraboloid with a superimposed solid body rotation.

The boundary condition at the tube wall, for the non-inertial co-ordinate system, is that of no slip:

$$(u, v, w) = 0 \quad \text{at} \quad \sqrt{(x^2 + y^2)} = 1. \tag{10}$$

In addition, the flow is symmetrical about the y axis:

$$u(x, y) = -u(-x, y), \quad v(x, y) = v(-x, y) \quad \text{and} \quad w(x, y) = w(-x, y) \tag{11}$$

and in particular

$$u = 0, \frac{\partial v}{\partial n} = 0 \quad \text{and} \quad \frac{\partial w}{\partial n} = 0 \quad \text{for } x = 0. \tag{12}$$

Equations (3)–(12) are sufficient to characterize laminar flow through the system. Owing to the symmetry of the flow it is only necessary to obtain the numerical solution for $x \geqslant 0$.

FINITE ELEMENT SOLUTION

The Bubnov–Galerkin method is used to approximate the solution of a penalty function formulation of the governing equations. Thus, the incompressible fluid is approximated as a slightly compressible one:

$$P = -\lambda(\mathbf{V} \cdot \mathbf{V}), \tag{13}$$

in which λ, the constant penalty parameter, is very large. In the light of equation (13) the incompressibility condition, i.e. the continuity equation, may be dropped. The success of this method relies on choosing an appropriate value for the penalty parameter. The larger the value of λ, the more the solution is penalized and the closer the incompressibility constraint is satisfied. If λ is too large, however, limitations in machine accuracy will lead to the destruction of the solution. In the present study a penalty parameter of 10^6 is employed in all computations.

In the finite element representation of the governing conservation equations the same interpolation function is used to approximate the behaviour of each of the three dependent variables. In the current approach nine-noded Lagrangian quadratic or second-order complete interpolation functions are employed over the isoparametric element domain. The use of the nine-noded element has been reported by Huyakorn et al.,[16] Bercovier and Engleman[17] and Bar Yoseph et al.,[18] to increase the smoothness and accuracy of convective flow solutions.

Specification of the interpolating functions leads to implementation of the Bubnov–Galerkin weighted residual criteria. This involves substitution of the interpolating functions into the penalized governing conservation equations, weighting each term by these functions and then integrating over the element area. The boundary conditions are invoked via the application of Green's theorem on the second-order terms, which also serves to reduce the order of the governing equations. The resulting equations are

x-component:

$$\int_{D^e} \left(u \frac{\partial [N_i]}{\partial x} \{u_i\} + v \frac{\partial [N_i]}{\partial y} \{u_i\} \right) [N_k] \, \mathrm{d}D^e$$
$$+ \int_{D^e} \left(\frac{\partial [N_i]}{\partial x} \frac{\partial [N_k]}{\partial x} + \frac{\partial [N_i]}{\partial y} \frac{\partial [N_k]}{\partial y} \right) \{u_i\} \, \mathrm{d}D^e \tag{14}$$
$$+ \lambda \int_{D^e} \left(\frac{\partial [N_i]}{\partial x} \frac{\partial [N_k]}{\partial x} \{u_i\} + \frac{\partial [N_i]}{\partial x} \frac{\partial [N_k]}{\partial y} \{v_i\} \right) \mathrm{d}D^e = 0,$$

y-component:

$$\int_{D^e} \left(u \frac{\partial [N_i]}{\partial x} \{v_i\} + v \frac{\partial [N_i]}{\partial y} \{v_i\} \right) [N_k] \, dD^e$$

$$- \frac{N_A}{2} \int_{D^e} [N_i][N_k] \{w_i\} \, dD^e \tag{15}$$

$$+ \int_{D^e} \left(\frac{\partial [N_i]}{\partial x} \frac{\partial [N_k]}{\partial x} + \frac{\partial [N_i]}{\partial y} \frac{\partial [N_k]}{\partial y} \right) \{v_i\} \, dD^e$$

$$+ \lambda \int_{D^e} \left(\frac{\partial [N_i]}{\partial y} \frac{\partial [N_k]}{\partial x} \{u_i\} + \frac{\partial [N_i]}{\partial y} \frac{\partial [N_k]}{\partial y} \{v_i\} \right) dD^e = 0,$$

z-component:

$$\int_{D^e} \left(u \frac{\partial [N_i]}{\partial x} + v \frac{\partial [N_i]}{\partial y} \right) \{w_i\} [N_k] \, dD^e$$

$$+ \frac{N_A}{2} \int_{D^e} [N_i][N_k] \{v_i\} \, dD^e \tag{16}$$

$$+ \int_{D^e} \left(\frac{\partial [N_i]}{\partial x} \frac{\partial [N_k]}{\partial x} + \frac{\partial [N_i]}{\partial y} \frac{\partial [N_k]}{\partial y} \right) \{w_i\} \, dD^e$$

$$= 4G \int_{D^e} [N_k] \, dD^e.$$

This set of equations corresponds to the kth node of the element. The integration is over the i nodes adjoining this kth node. The symbol $\{\ \}$ denotes a column vector, whereas $[N_i]$ signifies a row vector containing the interpolating polynomials.

Assembly of the element integral equations (14)–(16), results in a global sparse banded matrix equation. A 'reduced' Gaussian integration of order 2×2 is used for the penalty terms associated with the nine-node Lagrangian element. All other terms in the global matrix equation are evaluated using an 'exact' 3×3 integration order. The global matrix represents a system of simultaneous non-linear algebraic equations. The solution of this system is obtained using a modified version of the quadratically converging Newton–Raphson scheme. In order to reduce computational time the Jacobian matrix, in the modified method, is re-evaluated periodically rather than during every iteration. The specific details of the techniques employed in the present study are described by Noronha.[19]

RESULTS

All computations are performed in double precision on the University of Kentucky's IBM 3083 computer. The solution domain is divided into 51 elements, resulting in a total of 687 degrees of freedom (three per node). Further mesh refinement is not possible, owing to a limited core capacity of 2048 Kbytes. The basic mesh pattern consists of thirteen rays of unequally spaced nodes. The radial and tangential spacings are determined by the anticipated solution. A tighter packing is maintained near areas exhibiting steep velocity gradients, such as the central vortex region, whereas a coarser refinement is afforded near the line of symmetry for most of the results presented here. The numerical results are independent of the mesh pattern as long as rapidly changing regions are approximated with a sufficiently fine mesh.

As noted, previous studies have found that the laminar motion of a viscous fluid through a rotating non-aligned straight tube is characterized by the values of two dimensionless parameters: N_A^2 and ReN_A. In the current study, however, the governing equations are formulated in terms of N_A, an angular Reynolds number, and G, the dimensionless pressure drop across a length of pipe. In the limit of small Coriolis disturbances Berman and Mockros[5] have derived the following relationship between Re, the conventional axial Reynolds number, and G:

$$Re = G\left[1 - \left(\frac{G^2}{16,515,072} + \frac{1}{9216}\right)N_A^2\right].$$ (17)

Equation (17) is used in conjunction with the perturbation approximation of Berman and Mockros[5] as the initial guess required for the Newton–Raphson scheme in the present numerical study. Since this approximation is probably not valid for $N_A \gtrsim 40$ and $ReN_A \gtrsim 780$ alternative guesses have to be supplied in these regions. For example, although the perturbation approximation does not provide a very accurate solution for $N_A = 50$ and $G = 1$, it does provide a reasonable initial guess for the numerical solution since these fluid mechanical parameters are close to the estimated region of validity of the perturbation solution. In general, initial guesses are provided by using G as a continuation parameter for fixed values of N_A; solutions for $G = 1$, however, are obtained by using N_A as the continuation parameter. For the most part, the continuation parameter is increased by less than 100 per cent of its current value; the only exception occurs when G is small. This continuation process results in rapidly convergent solutions.

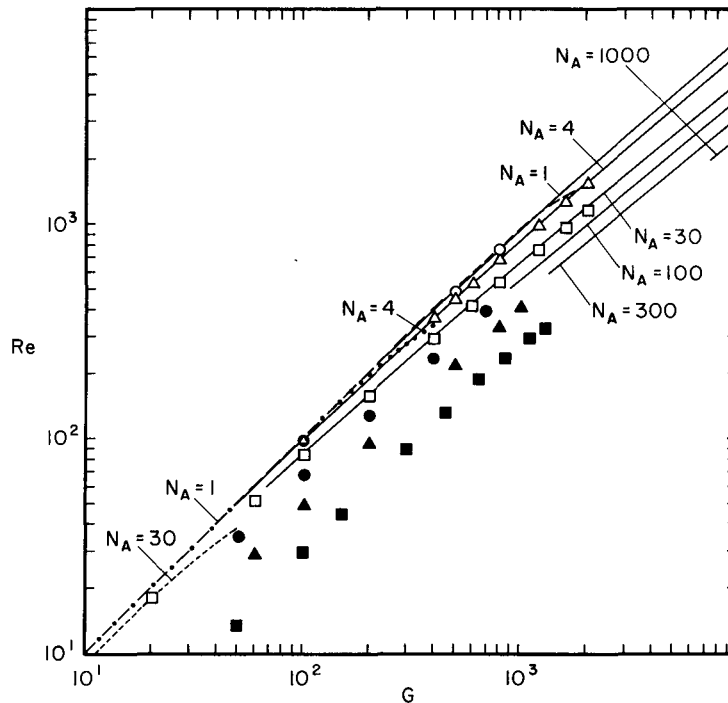The Reynolds number, Re, is plotted in Figure 2 as a function of G, the dimensionless axial

Figure 2. Reynolds number vs. dimensionless pressure drop. The data points are the numerical results of this study ($\bigcirc N_A = 1$, $\triangle N_A = 4$, $\square N_A = 30$, $\bullet N_A = 100$, $\blacktriangle N_A = 300$ and $\blacksquare N_A = 1000$). The broken lines are the theoretical results of Berman and Mockros[5] ($-\cdot-N_A = 1$, $\cdots N_A = 4$, $---N_A = 30$). The solid lines are the empirical results of Ito and Nanbu[10]

pressure drop in a rotating non-aligned straight tube. These results appear as a family of curves, with each curve corresponding to a particular angular Reynolds number. Included in this Figure are the numerical results of the present study (the data points), the theoretical results of Berman and Mockros[5] (the broken lines) and the relevant empirical results of Ito and Nanbu[10] (the solid curves). The numerical data shown in this Figure pertain to angular Reynolds numbers of $1, 4, 30, 100, 300$, and 1000, and values of G ranging from 10 to 2000. Figure 2 suggests that a larger pressure gradient is required to produce a particular flow through a rotating non-aligned straight tube than for a stationary straight tube. This may be explained by the fact that with rotation part of the energy which generates the flow is required to drive the secondary motion; the result is a reduction in the axial flux.

Figure 2 also indicates that the flow rates computed in the present study compare favourably with the theoretical results of Berman and Mockros[5] in the limit of mild Coriolis disturbances and the experimental results of Ito and Nanbu[10] for $N_A \lesssim 100$. The numerical data for $N_A = 300$ and $N_A = 1000$ are restricted to $G < 1000$ and $G < 1250$, respectively, whereas Ito and Nanbu's empirical relationship is valid at these angular Reynolds numbers for $G > 1330$ and $G > 7300$, respectively. Unfortunately the numerical solution is found to be mesh dependent for $N_A \geqslant 300$ and $G > 1300$. Presumably a finer mesh would correct this problem; however, core restrictions preclude such numerical experiments. In any event the trend of the numerical data suggests that the current solution predicts a greater friction loss than Ito and Nanbu's[10] experiments indicate for $N_A = 300, 1000$ and $G > 700$.

Conclusions regarding the region of agreement between the perturbation and numerical solutions can be made by comparing the two solutions on a node by node basis. Table I presents such a comparison for flow regimes that fall within or near $N_A \lesssim 40$ and $Re\, N_A \lesssim 780$, i.e. the estimated region of validity of the perturbation solution of Berman and Mockros.[5] Included in this table are entries for the numerically computed Reynolds number and the percentage two-norm difference between the individual velocity components obtained from the perturbation and numerical solutions. The percentage two-norm difference is computed from the following expression:

$$\text{Percentage error} = \left[\frac{\sum_{i=1}^{N} (\phi_i - \phi_i^{P})^2}{\sum_{i=1}^{N} (\phi_i^{P})^2} \right]^{1/2} \times 100 \qquad (18)$$

in which N is the total number of nodes and ϕ_i and ϕ_i^{P} are the numerical and perturbation

Table I. Percentage error norms between the numerical and perturbation solutions

N_A	G	Re	$Re\, N_A$	Percentage error norms			
				u	v	w	Total
1	1	0·99	0·99	4·5	1·8	0·2	0·2
1	100	99	99	4·6	1·8	0·2	0·2
1	800	770	770	7·5	5·6	2·1	2·1
4	1	0·99	4	4·6	1·8	0·2	0·2
4	100	99	396	4·8	2·1	2·0	2·0
4	400	370	1480	57·1	58·9	29·3	29·3
30	1	0·9	27	14·5	14·2	3·6	3·8
30	20	18	540	24·8	25·2	7·5	7·8
40	5	4·40	176	55·1	60·7	11·7	12·9

solutions, respectively, of velocity component ϕ at node i. In addition the total percentage two-norm difference has been computed, which contains information regarding all of the degrees of freedom.

The results presented in Table I indicate that in some flow regimes the numerical and perturbation approximations of the axial velocity distribution are in agreement, even though the corresponding approximations for the transverse profiles differ significantly. This point is particularly evident in the case of $N_A = 30$ and $G = 20$, where the average pointwise difference between the numerical and perturbation axial distributions is only 7·5 per cent even though the difference for each of the transverse profiles is approximately 25 per cent. This occurs despite the fact that the three components of the equations of motion are solved simultaneously.

An explanation of these differences concerns the relative strengths of the primary and secondary velocity components. In the absence of the Coriolis disturbance the axial flow field in a stationary straight pipe appears as a paraboloid. As the Coriolis acceleration is introduced this paraboloid distorts due to the secondary motion. In the limit of mild Coriolis effects, however, the axial profile is essentially unaffected by the relatively weak transverse flow field. Thus, differences between the secondary velocity fields predicted by the numerical and perturbation approximations will not necessarily be manifested as a difference in the axial velocity component even though the three components are coupled. Therefore, as indicated in Table I, the average total difference between the two approximations is essentially a reflection of the close agreement between the predicted axial profiles and not the significant differences between the predicted secondary behaviours.

Berman and Mockros[5] argue that their perturbation approximation will not give accurate results for flow regimes in which $N_A \gtrsim 40$ and $ReN_A \geq 780$. This argument is based on an order of magnitude analysis of the individual terms of the velocity field expansions rather than a comparison with experimental data or other theoretical solutions. The results of the present numerical study, which presumably has wider range of applicability than the perturbation approximation, confirm this argument and imply that the overall region of validity of the approximation is slightly narrower than the original estimate of Berman and Mockros.[5] This estimate does, however, provide a fair description of the region of validity of the axial component of the approximation for reasons discussed above.

The present investigation provides information concerning the primary and secondary flow fields that arise as a result of weak to moderately strong Coriolis disturbances. This information, for the most part, is not available from the analyses of Berman and Mockros[5] or Ito and Nanbu.[10] Numerical solutions have been obtained for the flow regimes that have been presented in Figure 2. These solutions are characterized by the strength of the Coriolis acceleration.

The Coriolis acceleration has components in both the y and z co-ordinate directions (see Figure 1). In the case of positive rotation the y component, which is proportional to the axial velocity, is directed radially outwards, resulting in the outward acceleration of fluid along the line of symmetry. This is always true for flow in the positive axial direction. Continuity ensures that the outwardly streaming fluid will eventually return, in the negative y direction, along the wall of the pipe. Thus, the y component of the Coriolis acceleration, which is proportional to ReN_A, serves to drive the secondary motion in the cross-section of the tube. These transverse circulations, in turn, tend to push or skew the axial velocity profile radially outwards away from the axis of rotation.

The z component of the Coriolis acceleration (refer to equation (6)) is proportional to the negative of the y component of velocity. Near the axis of symmetry the y component of velocity is positive; therefore, the axial component of the Coriolis acceleration will be directed in the negative z direction. In the region near the wall of the tube, removed from the line of symmetry, the fluid is returning in the negative y direction, and hence the axial component of the Coriolis acceleration is orientated in the positive direction. Thus, the z component of the Coriolis acceleration, which is

proportional to N_A^2, tends to retard the axially flowing fluid in the vicinity of the line of symmetry and promote the flow in regions located off the centreline. As the axial component of the acceleration is increased, the single-peaked axial flow distribution is expected to flatten out along the lateral axis and eventually split into a symmetrical double-peaked hill with each peak residing in one half cross-section of the tube.

Axial velocity contours are presented in Figures 3(a–e) for different combinations of the governing parameters. The corresponding peak axial velocities, marked with a +, are also indicated in these Figures. These contours, which are normalized to the maximum axial velocity in the cross-section of the tube, have been smoothed with the aid of the Surface II software package.[20] The effect of the axial component of the Coriolis acceleration on the primary velocity contours is presented in Figures 3(a) and 3(b). The contours of Figure 3(a) ($N_A^2 = 900$ and $ReN_A = 27$) are the product of a relatively mild Coriolis disturbance. As a result they are essentially axisymmetric and very similar to the parabolic velocity distribution characteristic of Hagen–Poiseuille flow. Figure 3(b) ($N_A^2 = 90,000$ and $ReN_A = 150$) illustrates the effect of a two order of magnitude increase in the axial component of the Coriolis acceleration. Selectively increasingly this component of the acceleration leads to distortion of the single-peaked axisymmetric profile depicted in Figure 3(a). The distribution has stretched along the lateral axis of the cross-section. Thus, the axial velocity distribution has evolved into a symmetric, double-peaked hill with each peak lying roughly on the
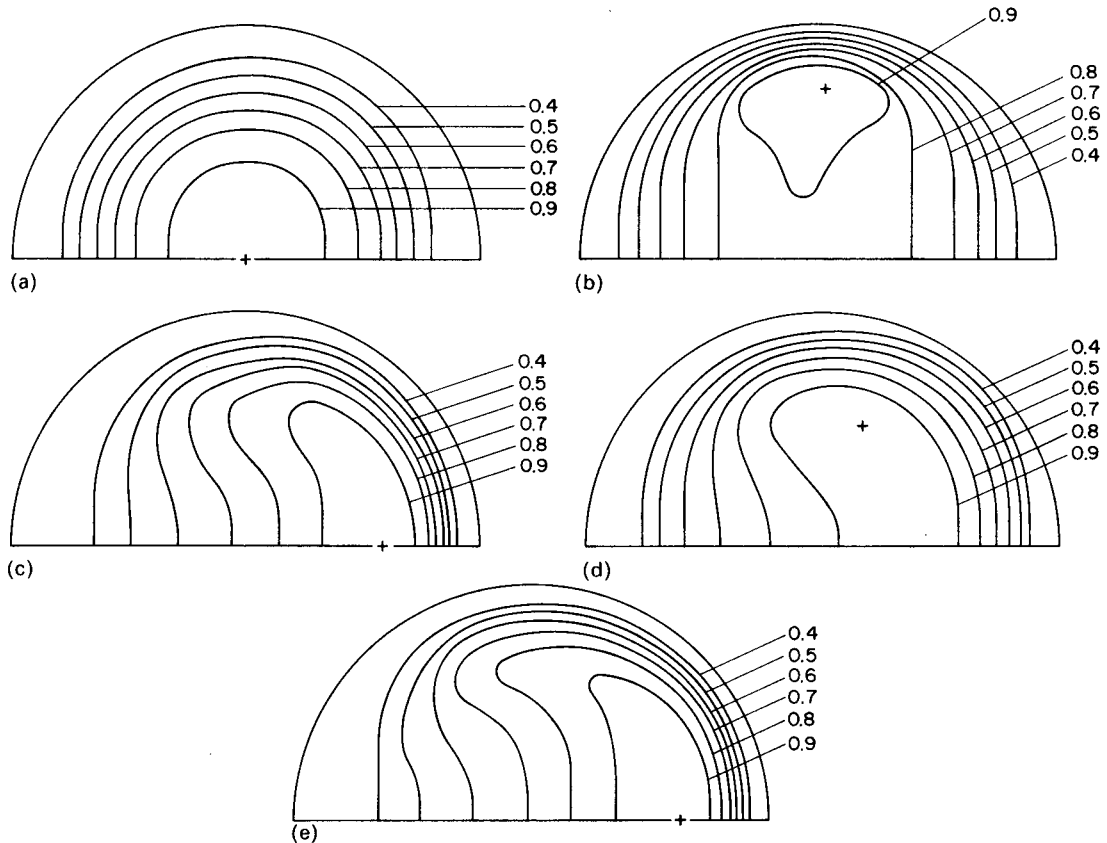

Figure 3. Normalized axial velocity contours: (a) $N_A^2 = 900$, $ReN_A = 27$ and $w_{max} = 0.851$; (b) $N_A^2 = 90,000$, $ReN_A = 150$ and $w_{max} = 0.369$; (c) $N_A^2 = 900$, $ReN_A = 16,300$ and $w_{max} = 479$; (d) $N_A^2 = 10,000$, $ReN_A = 6900$ and $w_{max} = 53.6$; (e) $N_A^2 = 10,000$, $ReN_A = 40,400$ and $w_{max} = 342$

lateral axis of the tube and close to the wall. The region near this wall is characterized by very steep velocity gradients. In the core, i.e. between the peaks, the axial velocity distribution is essentially uniform. This is similar to what Kheshgi and Scriven[15] found in square ducts for small Rossby and Ekman numbers.

Figures 3(a) and 3(b) confirm that the qualitative nature of the axial velocity distribution in a rotating non-aligned straight tube is significantly affected by the magnitude of the axial component of the Coriolis disturbance, i.e. N_A^2. Increasing this component tends to decelerate or retard the axially flowing fluid in the vicinity of the axis of symmetry and promote or accelerate its flow near the lateral walls of the tube. Thus, increasing N_A^2 while maintaining a relatively mild transverse component, i.e. ReN_A, tends to blunt the single-peaked axisymmetric paraboloid characteristic of Hagen–Poiseuille flow, and eventually split it into a symmetric double-peaked hill. As this occurs a boundary layer region develops near the lateral boundaries of the tube. The thickness of the boundary layer decreases as N_A^2 increases.

Figures 3(a) and 3(c) illustrate the effect of the transverse component of the Coriolis acceleration on the primary velocity distribution for flow regimes characterized by a relatively mild axial component. Figure 3(c) ($N_A^2 = 900$ and $ReN_A = 16,300$) represents slightly more than a one and a half order of magnitude increase in the transverse component of the Coriolis disturbance relative to the contours illustrated in Figure 3(a). These results indicate that, as ReN_A is increased, the axial velocity profile skews, along the axis of symmetry and away from the axis of rotation, toward the wall $\theta = 90°$. As this occurs a boundary layer region develops near the outer wall of the tube. This skewing is a direct consequence of secondary fluid motion which pushes the distribution radially outwards along the axis of symmetry. Since the secondary motion is driven by the transverse component of the Coriolis acceleration it is expected that the skewing effect should increase with ReN_A; this pattern is illustrated in Figures 3(a) and 3(c).

The axial velocity distributions that have been presented thus far have pertained to flow regimes in which both components of the Coriolis acceleration are negligible (Figure 3(a)) or either the axial component is dominant (Figure 3(b)) or the transverse component is dominant (Figure 3(c)). The relative magnitudes of the transverse and axial components of the Coriolis acceleration are characterized by the Rossby number, Re/N_A. A large value of the Rossby number indicates that the transverse component of the acceleration is more significant than the axial component, whereas a small value indicates that the converse is true. Figures 3(d) ($N_A^2 = 10,000$ and $ReN_A = 6900$) and 3(e) ($N_A^2 = 10,000$ and $ReN_A = 40,400$) illustrate the effect of increasing the Rossby number, i.e. the magnitude of the transverse component, as the axial component is maintained at a constant but significant level.

The contours presented in Figure 3(d) are characterized by Rossby number of 0·7. In this flow regime the axial component of the Coriolis acceleration only slightly dominates the transverse component, although both components are significant. Thus, the axial flow field exhibits both a distortion normal to the axis of symmetry and skewing outwards away from the axis of rotation. The point of maximum velocity is displaced from both the lateral and symmetry axes of the tube. The contours of Figure 3(e), on the other hand, are characterized by a Rossby number of 4. This flow regime is dominated by the transverse component of the Coriolis acceleration; it exhibits a single peak which lies on the axis of symmetry near the outer wall of the tube. Furthermore, it is seen that the axial velocity varies linearly across the core and very little from top to bottom. Keshgi and Scriven[15] noted similar behaviour for a rotating square conduit. The effect of the axial component of the Coriolis acceleration is not discernible for relatively high Rossby number flows. A summary of the fluid mechnical parameters relevant to Figures 3(a)–3(e) is presented in Table II.

In addition to the primary flow field the numerical solution enables an analysis of the transverse flow field. Transverse flow fields, corresponding to the axial contours of Figure 3, are depicted in

Table II. Summary of Figures

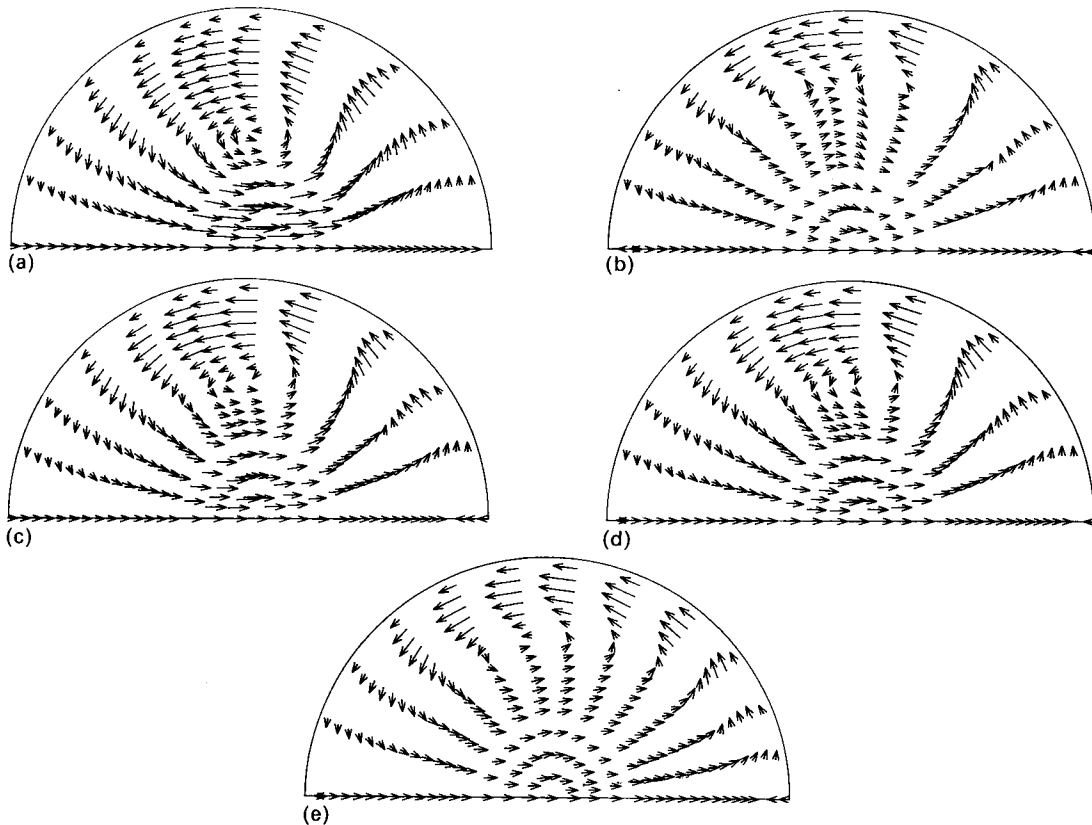| N_A	G	Re	N_A^2	ReN_A	Re/N_A	Figures
30	1	0·9	900	27	0·03	3(a), 4(a)
30	800	542	900	16,300	18·1	3(c), 4(c)
100	100	69	10,000	6900	0·7	3(d), 4(d)
100	700	404	10,000	40,400	4·0	3(e), 4(e)
300	1	0·5	90,000	150	0·002	3(b), 4(b)

Figure 4. Normalized transverse velocity vectors: (a) $N_A^2 = 900$, $ReN_A = 27$, $u_{max} = -0.0626$ and $v_{max} = 0.116$; (b) $N_A^2 = 90,000$, $ReN_A = 150$, $u_{max} = -0.0518$ and $v_{max} = -0.0987$; (c) $N_A^2 = 900$, $ReN_A = 16,300$, $u_{max} = -15.6$ and $v_{max} = -27.8$; (d) $N_A^2 = 10,000$, $ReN_A = 6900$, $u_{max} = -7.06$ and $v_{max} = -11.6$; (e) $N_A^2 = 10,000$, $ReN_A = 40,400$, $u_{max} = 22.6$ and $v_{max} = -41.6$

Figures 4(a)–(e) along with maximum u and v components of velocity. Each arrow in these Figures represents the resultant vector at a node normalized to the maximum resultant velocity vector in the particular flow field. Hence, the length of each arrow is a gauge of the magnitude of the resultant secondary velocity at that node relative to the other nodes in the flow domain.

The secondary velocity field presented in Figure 4(a) corresponds to the primary velocity field of Figure 3(a); it pertains to a flow regime driven by a relatively mild Coriolis acceleration. Thus, the secondary circulations are essentially symmetric with respect to the lateral axis of the tube with the centre of vortex motion lying somewhat closer to the axis of symmetry than the upper wall of the tube. Increasing the axial component of the Coriolis acceleration shifts the centre of vortex motion

along the lateral axis of the tube toward the upper wall. This effect is illustrated in Figure 4(b), which corresponds to the axial distribution of Figure 3(b). The secondary flow is approximately uniform and of mild intensity over much of the half cross-section. Near the lateral wall of the tube, however, the fluid must flow through the tight region between the centre of vortex activity and the wall. As a result, the velocities are most intense in this area. Overall, however, the secondary motion is fairly mild within the cross-section, since the transverse component of the Coriolis acceleration is very small. Thse results are qualitatively similar to those found by Keshgi and Scriven[15] for a square tube.

A few comments are appropriate concerning what appears to be a reversal of flow, in the corners, along the axis of symmetry in Figure 4(b) (as well as in the Figures that follow). The studies of Speziale[14] and Keshgi and Scriven[15] demonstrate that the double-vortex secondary flow in a rotating tube of rectangular cross-section splits into an asymmetric set of four counter-rotating vortices as the rotation rate is increased. This effect, which is known to occur in curved tubes, is attributed to a bifurcation of the solution. We feel that the flow reversals, evident in the corners of Figure 3(b), are a result of numerical artefact and, thus, do not suggest the appearance of an additional pair of vortices.

First, flow reversals are evident in both corners of Figure 4(b). Although Speziale[14] and Keshgi and Scriven[15] disagree on the side of the channel in which the additional vortex pair arises, there is no evidence that suggests the development of vortices in both corners of the flow domain. This is also true of numerical studies of curved tube geometries. Thus, if Figure 4(b) shows an additional vortex pair on the right side of the channel then the flow reversal in the left corner probably represents a numerical artefact or vice versa. Secondly, many of the solutions presented in Figure 4 have been recalculated using more elements along the axis of symmetry. None of these recalculated solutions lead to the disappearance of the flow reversals. Further investigation along these lines is limited by the available computer facilities. Finally, it is widely believed that the appearance of an additional vortex pair represents a bifurcation of the solution. This implies that two or more solutions are possible for one set of parameters. As stated previously our solutions are obtained by slightly incrementing the value of a continuation parameter and in all cases the resulting solutions rapidly converge. Studies concerning rotating and curved tubes report bifurcation of the solution when the continuation parameter is increased more than slightly. In addition, the bifurcation point is not characterized by a rapidly convergent solution. Thus, we believe that our results represent two-vortex solutions of the problem.

In theory the investigation of solution bifurcation is possible with the present code. In practice, however, many more elements are required. For example, Keshgi and Scriven[15] used a *minimum* of 441 nodes in their investigation of solution bifurcation in a rotating square cavity. Owing to storage capacity we were limited to a maximum of approximately 229 nodes, thus precluding an accurate study of bifurcation.

Figure 4(c) illustrates the effect, on the secondary fluid motion, of an increase in the transverse component of the Coriolis acceleration while the axial component is maintained at a low level; this profile corresponds to the axial distribution of Figure 3(c). As the transverse component is selectively increased the centre of vortex motion tends to shift, along the lateral axis of the tube, toward the upper wall. Finally, as both components of the Coriolis acceleration are increased, the centre of vortex motion shifts towards the upper wall of the tube and toward the axis of rotation. These effects are presented in Figure 4(e), which corresponds to Figure 3(e).

CONCLUSIONS

Through the use of finite element techniques it is possible to obtain solutions to a penalty function formulation of the equations which govern the laminar, fully developed, steady motion of a

Newtonian fluid through a rotating non-aligned straight tube. These results, which cover a wide range of flow regimes, compare favourably with the perturbation solution of Berman and Mockros[5] in the limit of mild Coriolis disturbances, and the experimental pressure drop measurements of Ito and Nanbu[10] for more intense accelerations. It appears that the qualitative and quantitative natures of the primary and secondary flow distributions depend on the relative magnitudes of the axial and transverse components of the Coriolis acceleration. These components are proportional to N_A^2 and ReN_A, respectively.

Furthermore, it should be mentioned that the flow fields which arise in a rotating non-aligned straight tube as a result of the Coriolis acceleration are qualitatively very similar to those which develop in coiled tubes, as a result of the centrifugal disturbance. In fact the parameters necessary to describe the motion of a fluid through a rotating non-aligned straight tube, N_A^2 and ReN_A, are analogous to the coil ratio and Dean number, respectively, in the coiled tube problem. Since the cylindrical geometry of a straight tube is easier to study than the toroidal-like geometry typically used to characterize coiled tubes, we feel that the present study can provide valuable insight into the more complicated coiled tube problem.

Extending our present penalty/Galerkin/finite element solution to include solution bifurcation is possible in theory but difficult in practice. Many additional elements would be necessary accurately to approximate the solution. The current work already uses most of the available space on our IBM 3083 computer. Thus, the advantage of the penalty/Galerkin/finite element method over more traditional finite difference schemes is questionable—at least for two-dimensional problems requiring fairly fine grids.

REFERENCES

1. P. A. Drinker, R. H. Bartlett, R. M. Bailer and B. S. Noyes, Jr., 'Augmentation of membrane gas transfer by induced secondary flow', *Surgery*, **66**, 775 (1969).
2. J. F. Murphy, 'Oxygen transfer into water or blood flowing in a rotating Coiled-Tube Membrane blood oxygenator', *Ph.D. Dissertation*, Theoretical and Applied Mechanics, Northwestern University, Evanston, IL, 1976.
3. J. Berman, 'A comparison of theoretical and experimental oxygen transfer into blood flowing through stationary and rotating helically coiled tubes', M. S. Thesis, Biomedical Engineering, Northwestern University, Evanston, IL, 1979.
4. J. Berman and L. F. Mockros, 'Oxygen transfer to water or blood flowing in a rotating non-aligned straight pipe', *ASME Bioengineering and Fluids Engineering Conference*, University of Houston, Houston, TX, 1983.
5. J. Berman and L. F. Mockros, 'Flow in a rotating non-aligned straight pipe', *J. Fluid Mech.* **144**, 297–310 (1984).
6. J. Berman and L. F. Mockros, 'Mass transfer to fluids flowing through rotating non-aligned straight tubes', submitted to *Journal of Biomechanical Engineering* (1985).
7. S. N. Barua, 'Secondary flow in a rotating straight pipe', *Proc. Royal of London, Series A*, **227**, 133–139 (1954).
8. G. S. Benton, 'The effect of the Earth's rotation on laminar flow in pipes', *J. Appl. Mech.*, **23**, 123–127 (1956).
9. Y. Mori and W. Nakayama, 'Convective heat transfer in rotating circular pipes (1st report, laminar region)', *International Journal of Heat and Mass Transfer*, **11**, 1027–1040 (1968).
10. H. Ito K. Nanbu, 'Flow in rotating straight pipes of circular cross section', *Trans. ASME D:J. of Basic Engineering*, **93**, 383–394 (1971).
11. Kamyar Mansour, 'Laminar flow in a slowly rotating straight pipe', *Journal of Fluid Mechanics*, **150**, 1–21 (1985).
12. B. S. Benton and D. Boyer, 'Flow through a rapidly rotating conduit of arbitrary cross-section', *J. Fluid Mech.*, **26**, (1), 69–79 (1966).
13. P. W. Duck, 'Flow through rotating pipes of circular cross-section', *Phys. Fluids*, **26**, (3), 614–618 (1983).
14. C. G. Speziale, 'Numerical study of viscous flow in rotating ducts', *J. Fluid Mech.*, **122**, 251–271 (1982).

15. H. S. Kheshgi, and L. E. Scriven, 'Viscous flow through a rotating square channel', *Phys. Fluids*, **28**, (10), 2968–2979 (1985).
16. P. S. Huyakorn, C. Taylor, R. L. Lee and P. M. Gresho, 'A comparison of various mixed interpolation finite elements in the velocity–pressure formulation of the Navier–Stokes equations, *Comput. Fluids*, **6**, 25 (1978).
17. M. Bercovier and M. S. Engleman, 'A finite element for the numerical solution of viscous incompressible flows', *J. Compt. Phys.*, **30**, 181–201 (1979).
18. P. Bar-Yoseph, J. J. Blech, and A. Solan, 'A finite element solution of the Navier–Stokes equations in rotating flow', *Int. j. numer. methods eng.*, **17**, 1123–1146 (1981).
19. W. P. Noronha, 'A finite element solution of flow through a rotating non-aligned straight tube', *M. S. Thesis*, Department of Chemical Engineering, University of Kentucky, Lexington, KY, 1984.
20. R. J. Sampson, *Surface II Graphics System*, Kansas Geological Survey, Lawrence, KS, 1975.